



Pulsational Pair-instability Supernovae. II. Neutrino Signals from Pulsations and Their Detection by Terrestrial Neutrino Detectors

Shing-Chi Leung^{1,2} , Sergei Blinnikov^{1,3,4} , Koji Ishidoshiro⁵ , Alexandre Kozlov¹ , and Ken'ichi Nomoto¹ 

¹ Kavli Institute for the Physics and Mathematics of the Universe (WPI), The University of Tokyo Institutes for Advanced Study, The University of Tokyo, Kashiwa, Chiba 277-8583, Japan; shingchi.leung@ipmu.jp, sblinnikov@gmail.com, kozlov@awa.tohoku.ac.jp, nomoto@astron.s.u-tokyo.ac.jp

² TAPIR, Walter Burke Institute for Theoretical Physics, Mailcode 350-17, Caltech, Pasadena, CA 91125, USA

³ NRC “Kurchatov Institute”—ITEP, B.Chernomushkinkaya 25, 117218 Moscow, Russia

⁴ Dukhov Automatics Research Institute (VNIIA), Suschevskaya 22, 127055 Moscow, Russia

⁵ Research Center for Neutrino Science, Tohoku University, Sendai 980-8578, Japan; koji@awa.tohoku.ac.jp

Received 2019 September 22; revised 2019 December 13; accepted 2019 December 14; published 2020 January 28

Abstract

A Pulsational Pair-instability supernova (PPISN) evolves from a massive star with a mass $\sim 80\text{--}140 M_{\odot}$ that develops electron–positron pair-instability after hydrostatic He-burning in the core has finished. In Leung et al. (Paper I), we examined the evolutionary tracks and the pulsational mass-loss history of this class of stars. In this paper, we analyze the thermodynamical history to explore the neutrino observables of PPISNe. We compute the neutrino light curves and spectra during pulsation. We then study the detailed neutrino emission profiles of these stars and estimate the expected neutrino detection count for different terrestrial neutrino detectors, including, e.g., KamLAND and Super-Kamiokande. Finally, we compare the neutrino pattern of PPISN with other types of supernovae based on a canonical 10 kt detector. The predicted neutrino signals can provide an early warning for telescopes to trace for the early time optical signals. The implications of neutrino physics on the expected detection are also discussed.

Unified Astronomy Thesaurus concepts: [Supernova neutrinos \(1666\)](#); [Stellar pulsations \(1625\)](#); [Supernovae \(1668\)](#)

1. Introduction

1.1. Pulsational Pair-instability Supernova

Pulsational pair-instability supernova (PPISN) is the explosion of a massive star by the instabilities during its pulsation. This occurs in a star with a mass from ~ 80 to $\sim 140 M_{\odot}$, where the exact mass is metallicity dependent. After He-burning, the massive C+O core experiences pair-creation instabilities (Barkat et al. 1967), where energetic photons that support the star are forming electron–positron pairs catastrophically during its contraction. Such a core can form when the metallicity is sub-solar ($\sim 0.8 Z_{\odot}$), where the massive star can develop a He-core above $40 M_{\odot}$. The stellar wind mass loss is suppressed during the main-sequence phase (Hirschi 2017; Limongi 2017; Leung & Nomoto 2018). The conversion of photons drastically lowers the radiation pressure, making the adiabatic index $< 4/3$. This makes the star enter an over-compressed state. Explosive O-burning is triggered, which makes the star rebound and pulsate. Depending on the pulsation strength, which increases with the stellar mass, a PPISN may eject a significant fraction of mass. After that, the star expands and relaxes. The star gradually contracts by losing energy through radiation and neutrinos (Woosley 2017), after which the star resumes its contraction. Depending on the amount of unburnt O left behind by the previous explosive O-burning and its replenishment from the outer zone by convective mixing, the star can carry out the above process repeatedly until the core runs out of O. At that point, the star collapses as a core-collapse supernova (CCSN). The combination of thermo-nuclear runaway and core collapse in one single star makes this class of stars interesting. We refer readers to Heger & Woosley (2002), Ohkubo et al. (2009), Yoshida et al. (2016a), Woosley (2017, 2018), Marchant et al. (2019), and Leung et al. (2019a) for some recent calculations of the PPISN pulsations and progenitor modeling of PPISNe.

PPISN is less studied than other types of supernovae due to its numerical complexity. It contains dynamical phases and quiescent phases. The dynamical phase occurs during pulsations where the dynamical timescale becomes shorter than the nuclear reaction timescale. The quiescent phase occurs between pulses, where the Kelvin–Helmholtz timescale determines the contraction time. It is difficult to follow its overall evolution with a single code. Multiple codes are used (see, e.g., Yoshida et al. 2016a) or an excerpt of the pulsation is followed (see, e.g., Chen et al. 2014). Recent development of the stellar evolution code Modules for the Experiments in Stellar Astrophysics (MESA; Paxton et al. 2011, 2013, 2015, 2017) allows flexible changes between the hydrostatic approximation for the quiescent phase and the implicit hydrodynamics calculations for the dynamical phase.

Despite the difficulty, PPISNe are important because they are one of the robust mechanisms for producing super-luminous supernovae. The massive mass loss during pulsation creates a rich circumstellar medium (CSM). They are also one of the channels for forming massive black holes ($\sim 30\text{--}50 M_{\odot}$) where the merger events of such black holes can generate gravitational-wave signals detected by, for example, advanced LIGO and VIRGO (Belczynski et al. 2017). During the final explosion when the Fe-core collapses, the ejecta interacts with the CSM and creates shock breakout. Such a process could produce a very bright event that would explain some super-luminous supernovae, including, e.g., PTD12dam (Sorokina et al. 2016; Tolstov et al. 2017), Eta Carinae (Woosley 2017), and iPTF14hls (Woosley 2018).

1.2. Neutrino as Another Messenger of Supernovae

In this and the coming decades, the increasing size of neutrino detectors has made probing neutrinos from the astrophysical sources possible. For example, the upgrade of

Table 1
The Characteristics of Some Recent Neutrino Detectors

Detector	Location	Mass (kt)	Detection Type	Medium	Main Neutrino Detected	Others
KAMLAND	Japan	1	liquid scintillator	organic liquid	$\bar{\nu}_e$	
SNO+	Canada	0.78	liquid scintillator	organic liquid	ν_e	
Borexino	Italy	0.278	liquid scintillator	organic liquid	ν_e	
JUNO	China	20	liquid scintillator	organic liquid	$\bar{\nu}_e$	
RENO-50	Korea	18	liquid scintillator	organic liquid	$\bar{\nu}_e$	
Super-Kamiokande	Japan	32.5	Water Cerenkov detector	H ₂ O	$\bar{\nu}_e$	With Gd
Hyper-Kamiokande	Japan	220	Water Cerenkov detector	H ₂ O	$\bar{\nu}_e$	With Gd
DUNE	USA	40	liquid argon detector	Liquid Ar	ν_e	

Table 2
The Stellar Evolutionary Models Prepared by the MESA Code

Model	M_{ini}	M_{fin}	M_{He}	M_{C}	M_{O}	Weak Pulse	Strong Pulse	Ejected Mass
He40A	40	37.78	6.79	3.13	27.5	5	1	2.22
He45A	45	39.26	7.38	4.03	31.3	3	1	5.74
He50A	50	47.39	7.82	4.16	35.2	1	1	2.61
He55A	55	48.22	8.27	4.30	39.0	1	1	6.78
He60A	60	51.48	8.69	4.43	42.9	0	2	8.52
He62A	62	49.15	8.77	4.59	44.6	0	2	12.85
He64A	64	0	8.96	4.63	46.1	0	1	64.00

Note. M_{ini} and M_{fin} are the initial and final masses of the star. M_{He} and M_{CO} are the integrated helium and carbon–oxygen masses of the whole star before the dynamical phase starts. No hydrogen mass is given because we start the star as a bare He core. “Weak Pulse” and “Strong Pulse” refer to the numbers of the corresponding pulses in the evolutionary history. All masses are in units of solar mass.

the Super-Kamiokande to the Hyper-Kamiokande increases the detection mass from 32.5 kton (Simpson et al. 2019) to 220 kton, which is expected to be realized in the later half of 2020s. In terms of the energy range, the large neutrino detector ICECUBE can detect neutrinos with an energy up to PeV. This enables the detection of neutrino sources beyond the Sun and CCSNe to objects such as blazars and supernova remnants in compact stellar clusters (Bykov et al. 2015). The low neutrino interaction cross section with matter allows supernova neutrinos to likely be able to reach the Earth before photons. The arrival of neutrinos, if detected, can serve as an early warning signal, used by the SuperNova Early Warning System (Antonioli et al. 2004). Gravitational-wave signals can also serve as a similar early warning for merging compact stars. The gravitational-wave signal is significant in a binary system, but it is much weaker in the single-star scenario. On the other hand, the neutrino emission can be significant in both a single star event, during its thermonuclear explosion or its core collapse, and in binary-star interactions such as a binary neutron star merger event.

Large terrestrial detectors that have either been built or proposed include (1) liquid scintillator detectors (e.g., the Kamioka Liquid-scintillator Antineutrino Detector (KamLAND) in Japan (Suzuki 1999; Asakura et al. 2016), SNO+ in Sudbury, Canada (Andringa et al. 2016), Boron solar neutrino experiment (Borexino) in Gran Sasso, Italy (Bellini et al. 2014; Agostini et al. 2015), The Jiangmen Underground Neutrino Observatory (JUNO) in China, (An et al. 2016), RENO-50 in Korea (Seo 2015), and Low Energy Neutrino Astronomy (LENA) in Europe Wurm et al. 2012); (2) Water Cerenkov detector in Super-Kamiokande and Hyper-Kamiokande in Japan (Watanabe et al. 2009; Abe et al. 2011a, 2011b) and IceCube in South Pole

(Abbasi et al. 2011), (3) Gadolinium-loaded water Cerenkov detectors Super-Kamiokande and Hyper-Kamiokande (Beacom & Vagins 2004), and (4) liquid argon detector (the Deep Underground Neutrino Experiment—DUNE) in the USA (Acciarri et al. 2016). In Table 1, we provide more specific details on the characteristics of these detectors. Detectors designed to detect both electron and anti-electron neutrinos are included for comprehensiveness. These detectors provide a wide range of exposure cross sections for multiple types of neutrinos and reaction channels. The diverse locations of the neutrino detectors allow the supernova position to be measured by the time delay between neutrino detection among various detectors. Detection methods such as the triangulation method (Brdar et al. 2018) are proposed to identify the neutrino source to a sub-degree accuracy. However, it also requires absolute time synchronization between detectors and knowledge of the arrival time of the neutrino pulses. The limited number of events in each detector may cap the accuracy in determining the arrival time of the neutrino signals.

So far, neutrino signals from thermonuclear related supernovae have been largely studied, including SNe Ia (see, e.g., Kunugise & Iwamoto 2007; Odrzywolek & Plewa 2011; Wright et al. 2016, 2017b) and PISN (Wright et al. 2017a). CCSN is also a natural source of astrophysical neutrinos, but electron captures, neutron star cooling, and its accretion are the major production mechanisms. The neutrino signal contains information about the core (Suwa et al. 2019), which may complement its optical observable where the mass ejection occurs on the surface. As remarked above, PPISN could be an important source of neutrinos due to its lower mass compared to PISN while having a significant thermonuclear burning during pulsation. Its multiple pulses also offer more chances to

produce neutrinos compared to the single explosive event in the other two types of supernovae.

1.3. Motivation

To our knowledge, there is not yet any systematic study about neutrino signals from PPISNe. In this work, we explore the neutrino signature including the neutrino luminosity and spectra based on our PPISN evolutionary models computed by MESA. We present our study about the typical features of neutrino signals emitted during pulsations in this class of supernovae.

In Section 2, we describe the code we used for preparing the stellar models. We then describe the numerical scheme for extracting the neutrino light curves and spectra. In Section 3, we present in detail the neutrino emission profiles and thermodynamical history of these models. In Section 4, we predict the expected neutrino detection rates by the existing and proposed neutrino detectors. Then, we compare the neutrino pattern with other types of supernovae. At last, we give our conclusions. In the Appendix, we compare the use of the analytic approximation to the numerical scheme we used for calculating the neutrino luminosity.

2. Methods

For the hydrodynamics model, we refer interested readers to Leung et al. (2019a, hereafter Paper I) for a detailed implementation. We used the stellar evolution code MESA version 8118 (Paxton et al. 2011, 2013, 2015, 2017) for computing the PPISN models from the main-sequence phase until the onset of Fe-core collapse. The implicit hydrodynamical scheme is used for following the pulsation of the star until the mass ejection is finished.

To reconstruct the neutrino emission history, we use the neutrino energy loss subroutine provided in MESA. It accounts for several major neutrino emission channels including pair-, photo-, plasma, and bremsstrahlung neutrinos, where the analytic formulas are given in Itoh et al. (1989).⁶ To calculate the neutrino spectra, we use the formulas given in Misiaszek et al. (2006) and Odrzywolek (2007), which contain the pair-annihilation and plasma neutrinos. We refer the readers to the original articles for the derivation of these formulas.

The number emission of the pair-neutrinos $\phi_{\text{pair}}(\epsilon)$ is given by the approximation

$$\phi_{\text{pair}}(\epsilon) = \frac{A}{k_B T} \left(\frac{\epsilon}{k_B T} \right)^{\gamma} \exp(-a\epsilon/k_B T). \quad (1)$$

Variables α , a , and A are fitting parameters where $\alpha = 3.180657028$, $a = 1.018192299$, and $A = 0.1425776426$. Notice that the fitting here assumes the matter is relativistic and non-degenerate, i.e., $kT > 2m_e$ and $kT > \mu_e$. In the presupernova scenario, such conditions may not be always satisfied. However, we argue that such an approximation will have small effects because its number emissivity scales directly with the total emissivity, which is dominated by the pair-annihilation rate. The emission spectrum is, to a good approximation, a thermal spectrum.

⁶ Open-source subroutines are available here: <http://cococubed.asu.edu/>.

To calculate the plasmon-neutrino spectrum and emissivity, we follow the prescription from Odrzywolek (2007), where

$$\phi_{\text{plasmon}} = Ak_B T m_i^6 \exp(-\epsilon/k_B T), \quad (2)$$

and

$$A = \frac{G_F^2 C_V^2}{8\pi^4 \alpha}. \quad (3)$$

In cgs units, $A = 2.115 \times 10^{30} \text{ MeV}^{-8} \text{ cm}^{-3} \text{ s}^{-1}$. Notice that one needs to take the corresponding C_V for electron-neutrinos and muon-/tau-neutrinos, respectively, for calculating pair-neutrinos.

The asymptotic transverse plasmon mass m_i is given by

$$m_i = \frac{4\alpha}{\pi} \int_0^\infty \frac{p^2}{E} (f_1 + f_2) dp, \quad (4)$$

where

$$f_i = \frac{1}{1 + \exp[(E + (-1)^i \mu)/k_B T]}, \quad (5)$$

which represents the Fermi–Dirac distributions of electrons ($i = 0$) and positrons ($i = 1$). In general, plasmon-neutrino is a less significant neutrino source compared to the pair-neutrino in the thermodynamics range in which we are interested.

3. Neutrino Signals

3.1. Review of Hydrodynamics Results

First, we review the hydrodynamical properties of the PPISNe presented in Paper I. In that work, we followed the evolution of the He cores from $40 M_\odot$ to $64 M_\odot$ from the main-sequence phase until the onset of core collapse using the MESA code. The pure He core assumes no metal at the beginning and thus resembles zero metallicity models. However, the metallicity does not affect the pulsation strength of a given He core mass, because it depends on the electron–positron pair-creation instabilities and the energy production of the explosion O-burning. These stars develop and form PPISNe after the massive He cores with masses $>40 M_\odot$ have formed. However, we remark that the capability of the star to form a He core massive enough for the PPISN event to occur depends on its mass-loss rate, which is dependent upon the stellar metallicity. When these stars are in a binary system, interaction with its companion star can affect the final He core mass before the onset of the pair-instability (Marchant et al. 2019). As reported in Paper I, the final He core mass can be as low as $30 M_\odot$ at solar metallicity, up to $45 M_\odot$ at one-tenth of solar metallicity.

The quasi-hydrostatic approximation is used for most parts of the simulations. Implicit hydrodynamics formalism is used while following the pulsation and mass-ejecting phases.

In Table 2, we list the PPISN models analyzed in this work. We list the global properties and the pulsation history of these models, where the stellar evolution is computed in Paper I. In all models, we classified two classes of pulsations: weak pulses and strong pulses. A weak pulse is the expansion of the core without any mass loss, while a strong pulse is that with mass loss. A weak pulse occurs often in a low-mass He core (below $50 M_\odot$). Above $50 M_\odot$, the first explosive O-burning is always strong enough to eject part of the surface or even matter in the CO layer. For a low-mass He core with $M_{\text{He}} < 55 M_\odot$, the pulsation can only eject about $1\text{--}2 M_\odot$ overall. For more massive He cores, especially

those close to the PISN limit ($M_{\text{He}} \sim 64 M_{\odot}$), a mass ejection above $10 M_{\odot}$ is possible. Accompanying the pulsations, the stellar luminosity can be 3–4 orders of magnitude higher than that during the quiescent phase.

In general, the number of weak pulses decreases when the He core mass increases. Conversely, there are more strong pulses when the He core becomes more massive. This is because, when the He core mass is closer to the pair-instability regime (i.e., $64 M_{\odot}$), the softening of the C+O core after the hydrostatic He burning is more significant. The level of compression until bounce, the amount of C+O matter burned in the process, and the released energy are higher. Thus, the strength of the pulse increases, which is more likely to eject more mass. We also refer the reader to Paper I for a description of the detailed physics of the pulsation history.

In all models, we treat $t = 0$ to be the moment when the first switch to implicit hydrodynamics starts. The switch to hydrodynamics is determined by the current timestep that the timestep is comparable with the Courant timestep. That means, when the onset of the pair-creation instability starts, the dynamical time gradually decreases as the density of the star increases. It becomes comparable or even shorter than the nuclear reaction timescale during the pulsation phase.

Different from stars of higher or lower masses, the core of a PPISN can exceed 10^9 K and then fall below that more than once as long as it pulsates, with its central density ranging from $\sim 10^5$ to 10^7 g cm^{-3} . The whole process can last for ~ 1 hr, and the hot stellar core emits an abundant amount of thermal neutrinos.

3.2. Neutrino Luminosity

In this section, we post-process the thermodynamics data from the simulations using MESA by the analysis described in Section 2. This means, based on the hydrodynamical results reported in Paper I for the density, temperature, and composition profiles of the He cores at different time slices, we reconstruct the total neutrino emission rates, neutrino luminosity in each channel, and the time-dependent spectra. We analyze three distinctive models, He40A, He50A, and He62A. We study their neutrino emissivities, average neutrino energies, and cumulative neutrino emission. Specific moments of the neutrino emission profiles are examined to understand how the star produces neutrinos.

The three models represent PPISNe with mild, moderate, and strong mass losses, which stand for different levels of mass ejections. We remark that model He40A is interesting because it demonstrates consecutive weak pulses before its last strong pulse. Such weak pulses largely delay the contraction, which allows the core to have a higher central density, which strongly enhances neutrino emission. Model He50A demonstrates the standalone strong pulse with a moderate mass ejection. Model He62A demonstrates the standalone strong pulse with a significant mass ejection near the PPISN-PISN transition.

In Figure 1, we plot the neutrino luminosities and their components for models He40A, He50A, and He62A. The typical neutrino luminosity is about $10^{46} \text{ erg s}^{-1}$ during the peak of the pulse. In all pulses, the pair neutrino is the major source of neutrinos, compared to other channels including the photon-neutrino and plasma-neutrino. Photo-neutrinos are always ~ 2 –3 orders of magnitude less than the pair-neutrinos, and the plasma neutrinos are another 2–3 orders of magnitude less. This suggests that considering only the pair-neutrino gives an accurate estimation of the total neutrino luminosity for the

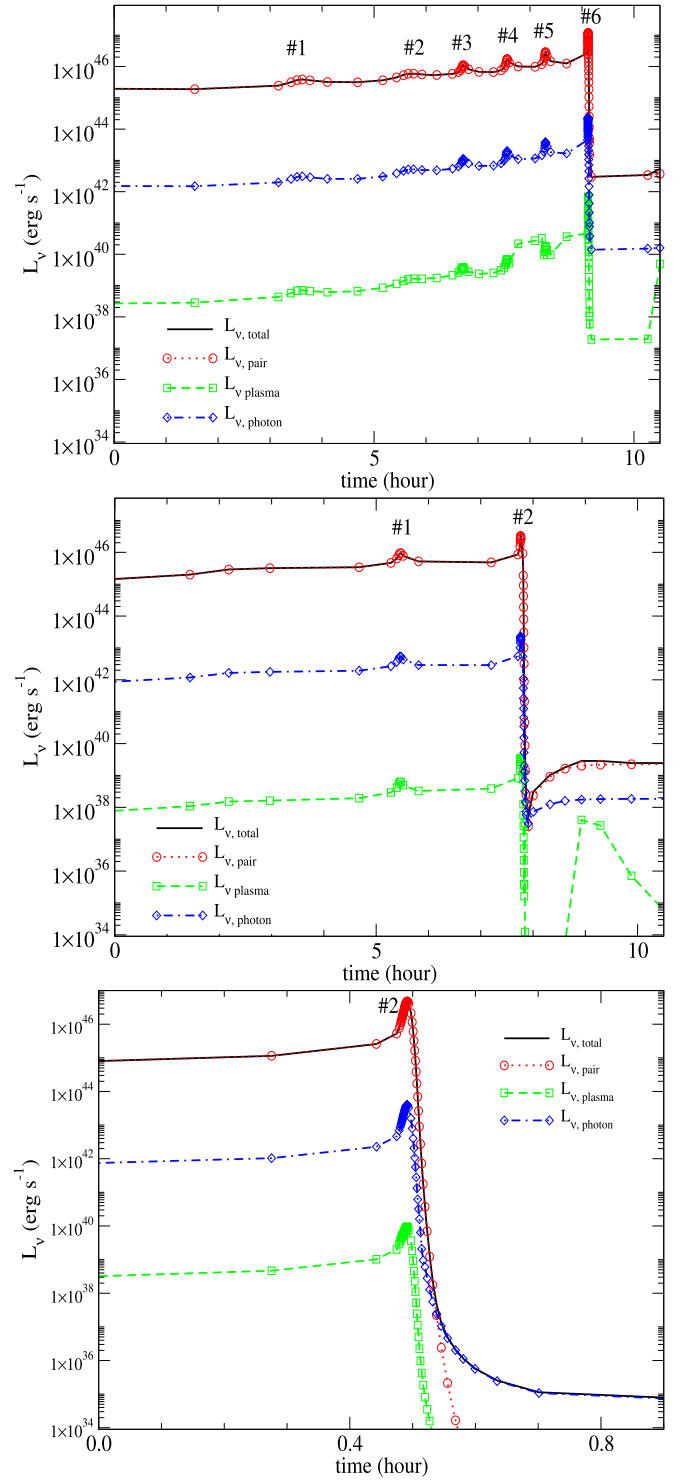


Figure 1. (Top panel) The neutrino luminosity and its components against time for model He40A, including the pair-, plasma, and recombination neutrino. All of the pulses before collapse are included. (Middle panel) Same as the top panel but for model He50A for all pulses. (Bottom panel) Same as the top panel, but for model He62A for the final pulse. In all three panels, zero time is defined by the start of the hydrodynamics, i.e., the beginning where the star becomes dynamical as it enters the pair-creation instabilities.

pulsations in PPISNe, which is consistent with that discussed in Blinnikov & Rudskii (1989). In the Appendix, we present a more detailed comparison between the tabular form and the analytic rates. During the quiescent phase, the neutrino

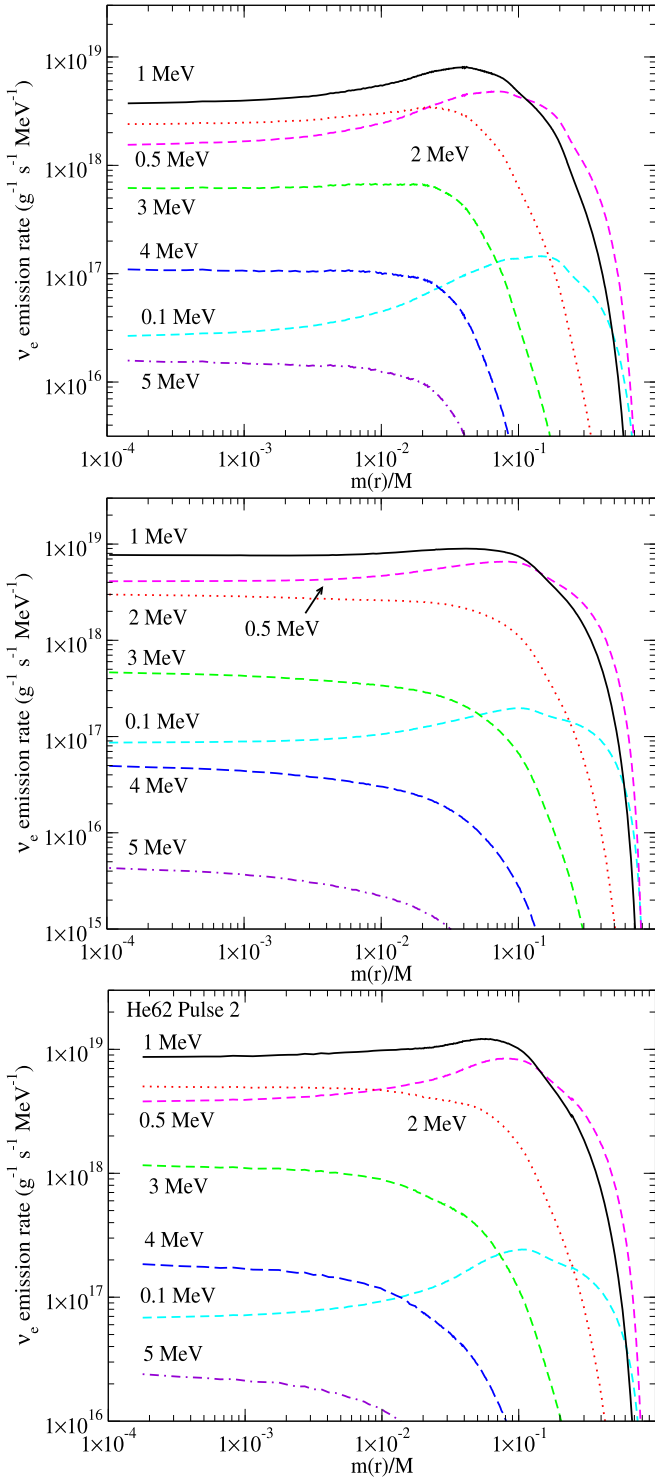


Figure 2. (Top panel) The neutrino spectra of model He40A at the peak of the final pulse for neutrinos with energies from 0.1 to 5 MeV. (Middle panel) Same as the top panel but at the peak of the final pulse for model He50A. (Bottom panel) Same as the left panel but at the peak of the final pulse for model He62A.

luminosity is negligible compared to its peak values, which can be 4–10 orders of magnitude higher.

3.3. Neutrino Spectra during Pulsation

In Figure 2, we plot the neutrino spectra of neutrinos with energies from 0.1 to 5 MeV, during the peak of the pulses for

the three mentioned models. The spectrum is a single snapshot obtained by integrating the neutrino emission in the whole star when the neutrino luminosity reaches its maximum during a pulse. The neutrino spectra include contributions of both pair-neutrinos and photo-neutrinos. By examining the patterns of the neutrinos, we can see that the neutrino emission, in most cases, remains thermal, so that the number emission drops when the neutrino energy increases. Below 1 MeV, the neutrino number drops rapidly. Neutrinos with an energy 0.1 MeV have neutrino numbers almost as low as those with an energy 5 MeV. In general, the energy threshold of current neutrino detectors is ~ 1 MeV, so the low-energy neutrinos are not counted as detected. Future generation-3 noble liquid-based neutrino detectors using argon, silicon, germanium, and xenon as the scintillator, such as DARWIN (Aalbers et al. 2016) and ARGO (Aalseth et al. 2018), can allow for much lower-energy thresholds based on the technique used in dark-matter detection (Raj et al. 2019). This increases the chance of capturing supernova neutrinos for distinguishing the supernova explosion mechanisms (Raj 2019).

By comparing the shape of the neutrino spectra, we show that the PPISN shares similar neutrino spectra where low-energy neutrinos (~ 1 MeV) dominate the emission, while higher-energy neutrinos (~ 5 MeV) can be 2–3 orders of magnitude lower. This shows that during pulsation, the core has only barely reached the temperature for producing thermal neutrinos. Nevertheless, the central temperature can be as hot as $10^{9.5-9.7}$ K. The neutrino production focuses mostly on $q = m(r)/M \approx 0.1$ for all three cases, as shown by the bumps for 1–2 MeV neutrinos. They are the places where very active burning takes places.

3.4. Neutrino Number Evolution during Pulsation

In Figure 3, we plot the energy-integrated neutrino number emission rate for the same set of models at the peaks of the pulses of models He40A, He50A, and He62A. The star emits neutrinos at a rate of $\sim 10^{50}$ s $^{-1}$ when the star contracts after the core has exhausted its He. Then, it quickly rises to $\sim 10^{52}$ – 10^{53} s $^{-1}$ when the core reaches its maximum compactness. Most neutrinos are emitted within 10^{-4} yr (~ 1 hr) up to the temperature peak reached by the core. Then, the neutrino emission quickly falls. This means that for most pulses, there is only one major outburst of neutrinos coming from the core, then the core expands and becomes too cold for further neutrino emission.

The duration where most neutrinos are emitted decreases when the progenitor mass increases. Model He40A shows an extreme extension. This is because, before its final pulse, the weak pulses do not expand the star or cool down the core. Thus, the neutrino emission continues, which provides a longer duration compared to the other five models. Model He50A shows a sharp peak of the neutrino flux before expansion. On the other hand, model He62A shows a smooth but rapid rise and fall in the neutrino emission rate.

3.5. Neutrino Spectra Evolution

We examine the evolution of neutrino spectra for the three models. In Figure 4, we plot the neutrino spectra as a function of time for the same set of models.

The typical neutrino number emission for each band follows a similar structure. It is because they depend on the same

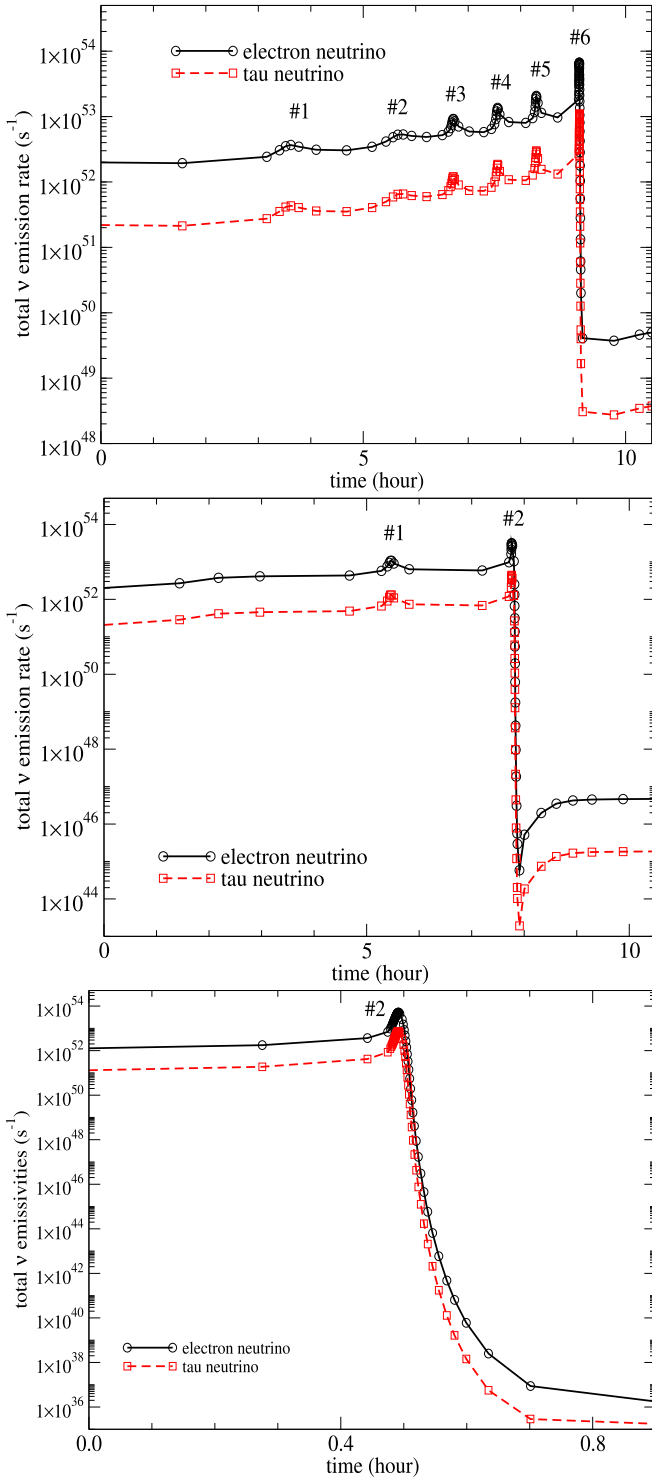


Figure 3. (Top panel) The neutrino number emission of model He40A at the peak of all pulses. (Middle panel) Same as the top panel but at the peak of all pulses for model He50A. (Bottom panel) Same as the top panel but at the peak of the final pulse for model He62A. The time convention follows Figure 1.

scaling relation in Equation (1). The neutrino emission increases during contraction and decreases during expansion. The typical emission number at the peak is $\sim 10^{53} \text{ s}^{-1} \text{ MeV}^{-1}$. The number emission rate typically drops by one order of magnitude when the neutrino energy increases by 1 MeV. Despite that the shape of the curve follows each other, showing

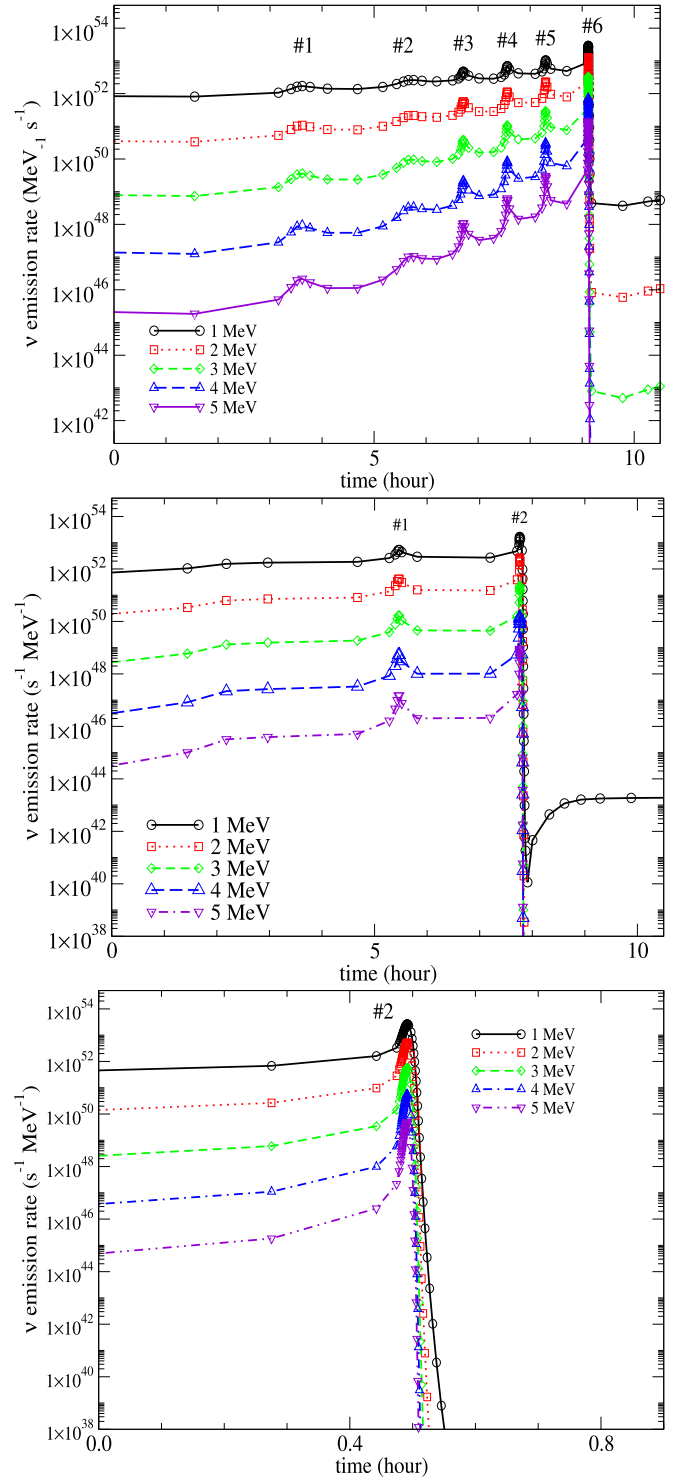


Figure 4. (Top panel) The neutrino number emission against time for neutrino energies from 1 to 5 MeV of model He40A. (Middle panel) Same as the top panel but for model He50A. (Right panel) Same as the top panel but at the peak of the second pulse for model He62A. The time convention follows Figure 1.

only thermal contributions. The contraction in models with a lower He core mass is slower; thus, the neutrino number emission rate exhibits more features. On the other hand, for a more massive He core, expansion follows immediately after contraction and the explosive O-burning; thus, the neutrino signal has only a one-peak feature.

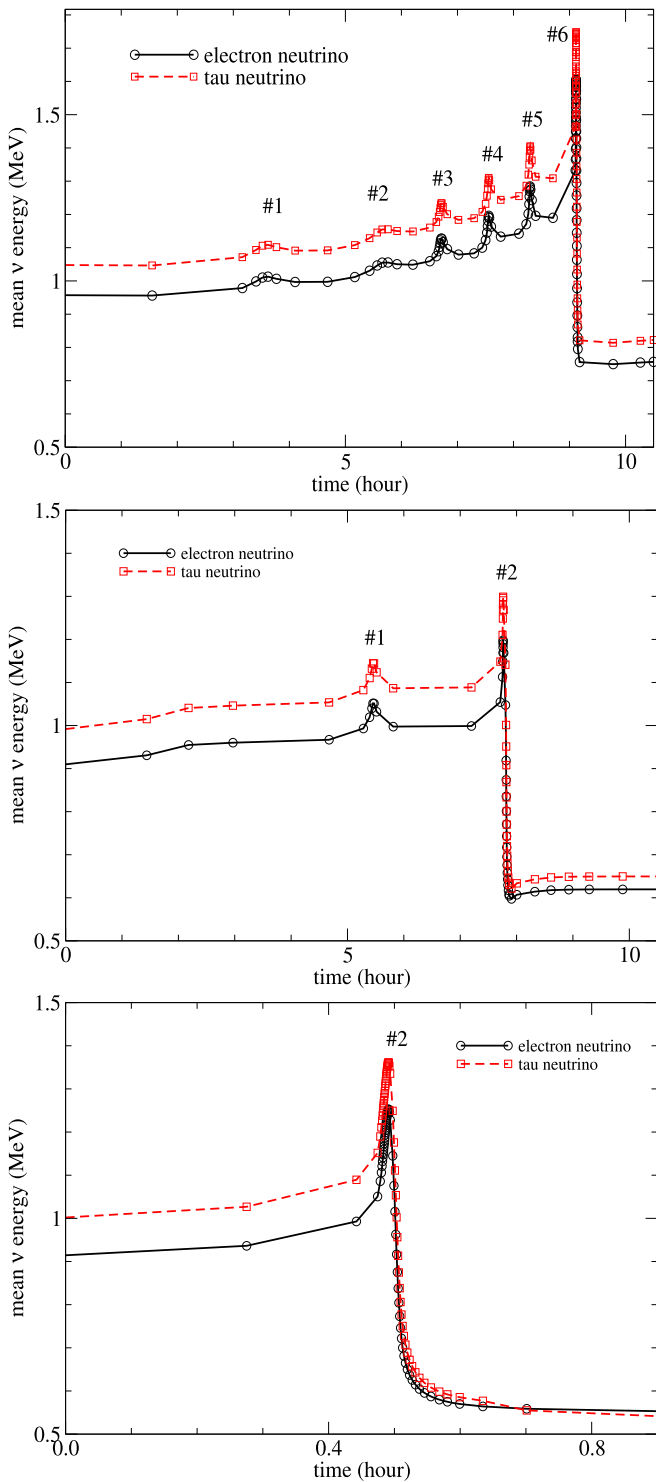


Figure 5. (Top panel) Mean neutrino energy against time for ν_e and ν_τ of model He40A for all pulses. (Middle panel) Same as the top panel but for model He50A for all pulses. (Bottom panel) Same as the top panel but at the peak of the second pulse for model He62A during the second strong pulse. The time convention follows Figure 1.

3.6. Neutrino Energy Evolution

At last, we examine the mean energy of both ν_e and ν_τ in our models. The mean energy is obtained by $\Sigma E_{\nu,i} n_{\nu,i} / \Sigma n_{\nu,i}$. In Figure 5, we plot the averaged neutrino energy of the three models for both ν_e and ν_τ as a function of time.

The ν_τ has always a higher mean energy than the ν_e . The typical neutrino energy is ~ 0.9 MeV in the quiescent time, and it increases to its peak ~ 1.1 MeV when the star is the most compact. The maximum mean energy of neutrinos decreases when the He core mass increases during the first peak. This is because when the He core is more massive, the corresponding central density becomes lower when the explosive O-burning is triggered. In the ρ - T diagram, the trajectory of the core is closer to the pair-creation instability zone.

3.7. Precollapse Neutrino Signal

In this section, we further examine the neutrino production of PPISN before its collapse. Unlike the pulsation, when the star finally runs out of ^{16}O for its explosive burning, the core is sufficiently massive that it promptly collapses. In this phase, although it can reach a higher central density and temperature, which is favorable for neutrino emission, the respectively shorter timescale also limits the number of neutrinos emitted. To demonstrate the similarity of the precollapse in different models, we consider the two contrasting models, namely, models He40A and He62A, to examine how the neutrino number flux and the energy distribution vary with time.

In Figure 6, we plot the neutrino number emission rate against time for both ν_e and ν_τ during the precollapse phase of the two models. The neutrino number emission becomes significant only at 0.001–0.002 yr (< 1 day) before the collapse. The two types of neutrinos can have their number emission rates increased by 2–3 orders of magnitude, until their peaks of $\sim 10^{53}$ erg s $^{-1}$, when the simulations stop. We do not evolve further because beyond that, nuclear physics and neutrino transport become important, but these physics components are not implemented in the stellar evolution code, when the density exceeds $\sim 10^{11}$ g cm $^{-3}$.

In Figure 7, we plot the mean neutrino energy against time for the two models. Unlike the mean energy in the pulses, the mean energy for both types of neutrinos can be higher as a result of higher central temperature ($\sim 10^{10}$ K) before collapse. This shifts the thermal spectra toward a higher energy, where at the peak, the neutrinos can have an average energy of ~ 3 MeV. No qualitative difference can be found between the two contrasting models.

In Figure 8, we plot the spectral evolution of the two models for neutrinos with an energy from 1.0 to 5.0 MeV. In the two models, a thermal-like distribution can be observed. The high-energy neutrino (5 MeV) is comparable with the low-energy neutrino (1 MeV) only at the moment very close to the onset of collapse.

4. Discussion

4.1. Predicted Neutrino Signals

4.1.1. Neutrino Energy Distribution

In this section, we examine the expected neutrino signals by the terrestrial neutrino detectors. We examine how the neutrino energy distributions look in all the three cases. They include the neutrinos produced during the weak pulse, the strong pulse, and in the precollapse phase. We want to examine if the energy distribution provides important indications that the neutrinos detected comes from the PPISN, instead of other possible background.

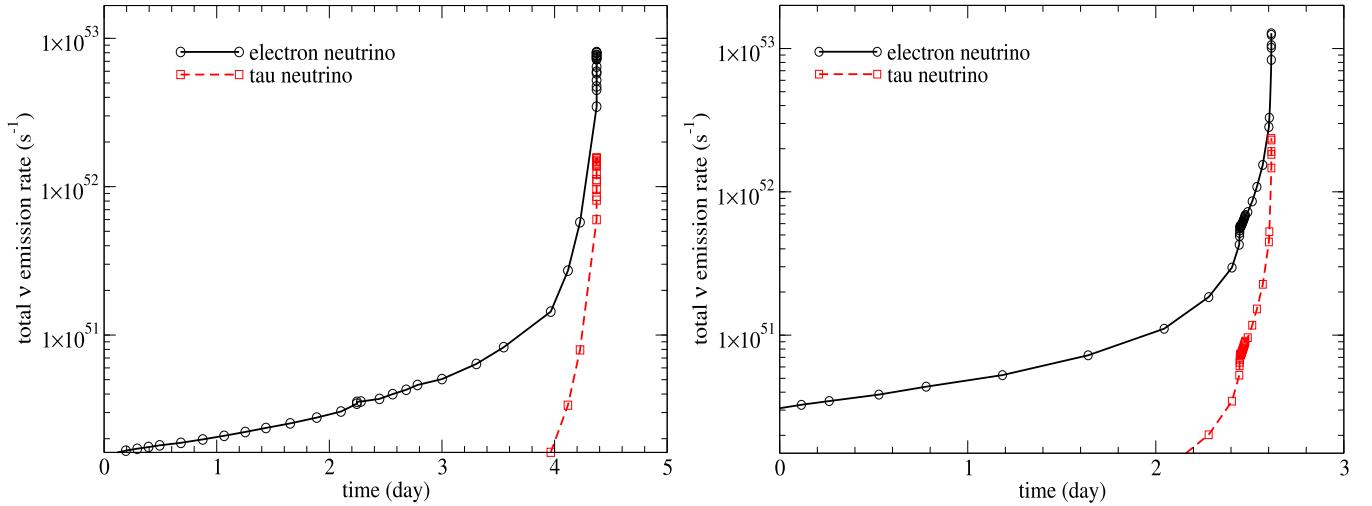


Figure 6. (Left panel) Neutrino number emission rate against time for ν_e and ν_τ before the onset of collapse of model He40A. (Right panel) Same as the left panel but for model He62A. In both panels, time 0 is shifted such that the relevant time range can be shown until the simulation ends.

To illustrate the difference, we consider model He40A and take three spectral snapshots at three moments, when the star has a maximum neutrino emission (1) in the second pulse (weak pulse), (2) at the sixth pulse (strong pulse), and (3) near the end of simulation (precollapse). They have neutrino number emission rates at 9.16×10^{52} , 6.68×10^{53} , and $8.08 \times 10^{52} \text{ s}^{-1}$, respectively. In Figure 9, we plot the spectra of these three moments. In the weak pulse, where the star is not globally heated by the explosive O-burning, the neutrino distribution is monotonically decreasing. In the strong pulse, the energy spectrum shows the form $\sim \exp(-E_\nu/k_B T)$. There is a peak emission around 1 MeV and then the emission rate quickly drops. There is a five-order-of-magnitude difference for neutrino numbers between energies of 1 and of 5 MeV. At last, in the precollapse moment, although it has, in total, a lower neutrino emission, the neutrino distribution extends to a higher energy. The peak shifts to ~ 2 MeV, with the 5 MeV neutrino being comparable with the lower-energy neutrinos.

From this comparison, one can see that despite that the neutrino spectra are collections of all of the fluid elements in the star, which have a wide range of density and temperature, the overall spectra are still comparable to the Boltzmann distribution. Furthermore, the low-energy neutrinos carry most of the thermal energy in the pulses, while neutrinos in a wider energy range can be found in the precollapse scenario.

In the above analysis, we have assumed that the neutrino directly reaches the Earth without any interaction. In fact, the neutrino oscillation and the mass hierarchy of neutrinos can play a role in the final neutrino count. The neutrino oscillation and resonances with leptons by Mikheyev–Smirnov–Wolfenstein effects may further alter the original neutrino sources. The mass hierarchy changes the rate of oscillation by its extra interaction term in the flavor eigenstate oscillation Hamiltonian. However, as shown in Wright et al. (2017b), the differences between the normal and inverted mass hierarchies are subtle. Given the uncertainties to the other parts of input physics, we expect that the difference among different mass models may be too small to be observed.

To estimate the astrophysical origin, we assume the star to be at 1 kpc from the Earth. This stands for a surface area about $1.20 \times 10^{44} \text{ m}^2$ for the neutrino flux. We remind the reader that, in fact, there exists massive stars near our neighborhood.

In Table 3, we tabulate some of the nearby stars which has a mass above $80 M_\odot$ and has a distance around 1 kpc. These stars can be the candidates for the future pulsation events when their He core mass grows to the mass range necessary for pair-instability.

4.1.2. Neutrino Number Counts

We have presented in Section 3.2 the detailed neutrino emission profiles and the history of the representative PPISN models. Here, we estimate the possible detection by terrestrial neutrino detectors. To estimate the detection counts, we use the following estimation. We assume the detection relies on the weak interaction $p(\bar{\nu}_e, e^+)n$, where the positron is quickly annihilated by surrounding electrons. The cross section is given by

$$\sigma = \frac{G_F^2 \epsilon_\nu^2}{(\hbar c)^4 \pi} (C_V^2 + 3C_A^2) \left(1 - \frac{Q}{\epsilon_\nu}\right) \quad (6)$$

$$\times \sqrt{1 - 2\frac{Q}{\epsilon_\nu} + \frac{Q^2 - m_e^2}{\epsilon_\nu} \Theta(\epsilon_\nu - Q)}, \quad (7)$$

where C_V and C_A are the vector and axial-vector coupling constants, G_F is the Fermi weak coupling constant, and ϵ_ν is the neutrino energy. $Q = 1.3 \text{ MeV}$ is the mass-energy difference between p and n and $m_e = 511 \text{ keV}$ is the electron mass. The step function arises naturally from the mass difference between n and p such that the interaction occurs only when the neutrino is sufficiently energetic. We assume that the canonical neutrino detector contains water with a mass of 10 kton. This represents $\sim 6.69 \times 10^{32}$ hydrogen atoms.

In Table 4, we tabulate the optimistic detection numbers for different current and proposed neutrino detectors. Rates below 1 count per minute are neglected. The neutrino source is assumed to be at 1 kpc. We assume a uniform energy bin of 0.5 MeV from 0.5 to 20 MeV. Due to the Heaviside function, neutrinos below $\sim 1.5 \text{ MeV}$ are cut off by default. We further assume a perfect detection rate for the neutrino detector. We do this because the actual detection accuracy depends on the energy threshold, the detection acceptance rate, and the energy reconstruction algorithm of individual neutrino detectors.

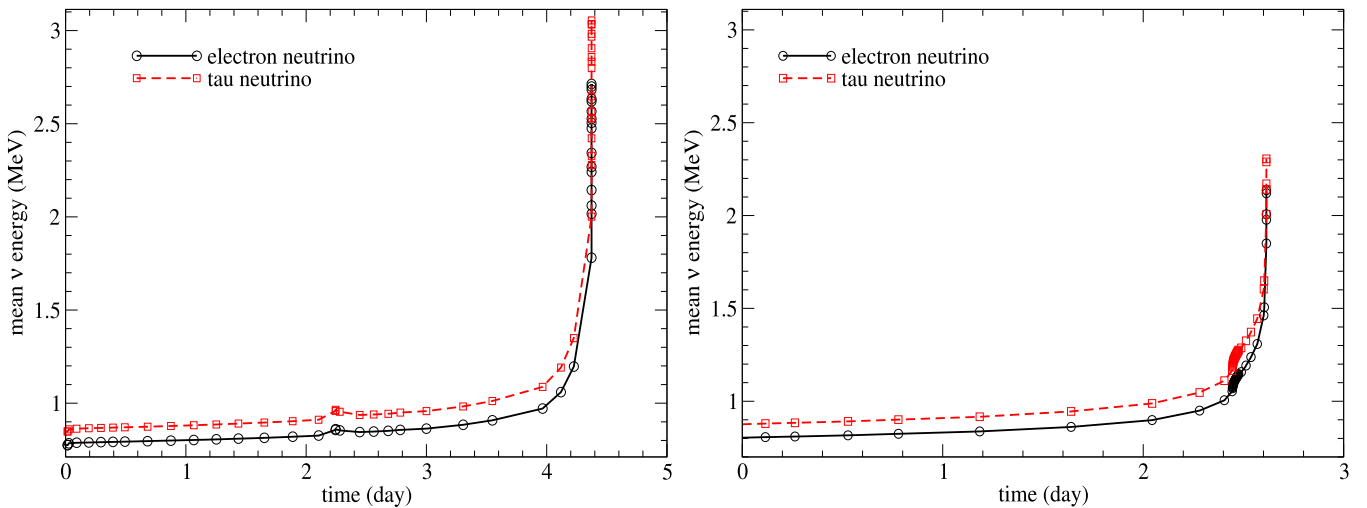


Figure 7. (Left panel) Mean neutrino energy against time for ν_e and ν_τ before the onset of the collapse of model He40A. (Right panel) Same as the left panel but for model He62A. The time convention follows Figure 7.

However, not all data is openly available. The energy threshold, in particular, is detector-dependent. For example, LENA (Wurm et al. 2015) is proposed to have a threshold energy as low as 2 MeV. On the other hand, the threshold energy for ICECUBE can be as high as 200 TeV (Aartsen et al. 2016). The incoming neutrinos from PPISN will be shielded by noise in ICECUBE, but they can be detected by LENA. As a first approximation, we assume the detector has a perfect detection rate. Current neutrino detectors such as KamLAND, SNO+, and Borexino are on the lower side of detection counts that can detect neutrinos produced in model He40A; on the other hand, most current detectors cannot detect any significant number of neutrinos emitted from more massive star models. Future neutrino detectors such as JUNO and LENA can detect more neutrinos on the order of $O(10)$. Super-Kamiokande and Hyper-Kamiokande can predict the highest amount of neutrinos from ~ 10 to ~ 100 .

Based on the above methods, in Figure 10, we plot the cumulative ν_e count of each strong pulse for models He40A, He50A, and He62A per 1 kton of the detecting material for an astrophysical source at a distance of 1 kpc. The cumulative sum is assumed to count across each pulse individually. Based on the number of strong pulses experienced in the models, the cumulative counts differ slightly. Most neutrinos are detected within 0.002 yr (\approx day). The following expansion of the supernova no longer produces an observable amount of neutrinos. To connect with the results in Table 4, we need to multiply the results in the figure by the mass of the neutrino detector and divide the distance squared in units of kpc.

For a lower-mass He core ($40\text{--}55 M_\odot$), there is only one strong pulse; as a result, the core tends to be more compact when it stops contraction and starts its expansion. The typical density of the star is higher, thus allowing more neutrinos to be generated. The total number detected by the model neutrino detector, assumed to be 1 kpc away from the supernova and have a detection mass of 1 kton, is higher. It has a typical value of $O(10^1)$ across the pulsation, and the total number decreases with mass.

For a higher-mass He core ($55\text{--}62 M_\odot$), there are two strong pulses. The first pulse occurs very soon in the contraction phase because of the abundant ^{16}O in the core. Therefore, the corresponding density and temperature of the star is lower. The

typical neutrino count is lower, $\sim 10^6 \text{ kton}^{-1}$ across the event. On the other hand, in the second pulse, because the core has much less ^{16}O than the first pulse, the core needs to reach a more compact state during contraction in order to make the outer core where ^{16}O is not yet burned during the first pulse. There are more neutrinos detected during the pulsation. Despite that, the total neutrinos detected are still fewer than those from its lower-mass counterpart.

4.2. Comparison with Other Types of Supernovae

The possibility of using neutrinos as a precursor to detect the emergence of a supernova has been proposed in the literature. The early light curve can provide important information about the outer structure of the star, which cannot be easily detected (Bersten et al. 2018). It occurs very soon after the explosion, in the scale of shock crossing time of the envelope. It requires coincidences for orienting the telescope to the supernova hosting galaxy right at the moment where the explosion starts, if no early warning signal is provided. On the contrary, when the associated neutrinos can be detected, there is a time delay between the arrival of neutrino and photons. The shock propagates at a sub-light-speed velocity toward the surface, compared with the neutrinos traveling in the speed of light. The difference can be varying from a few seconds (for a SN Ia), to a few minutes (for a blue supergiant), and up to as much as a \sim hours (for a red supergiant). See, for example, Dessart et al. (2017) and Owocki et al. (2019) for recent theoretical predictions of shock breakout in massive stars and Garnavich et al. (2016) for a recent observation of the early time light curve demonstrating shock breakout in a massive star explosion. The optical evolution of these shock breakout events contains very useful information about the pre-explosion structure of the star. Additionally, the neutrinos detected contain information directly from the stellar core.

In Table 5, we compare the neutrino luminosity, energy, and detection counts for different types of supernovae. E_ν is the average neutrino energy per particle and L_ν is the total neutrino luminosity.

SN Ia, as an explosion by thermal nuclear runaway in a carbon–oxygen or oxygen–neon–magnesium white dwarf, can generate neutrino by both thermal processes and electron captures.

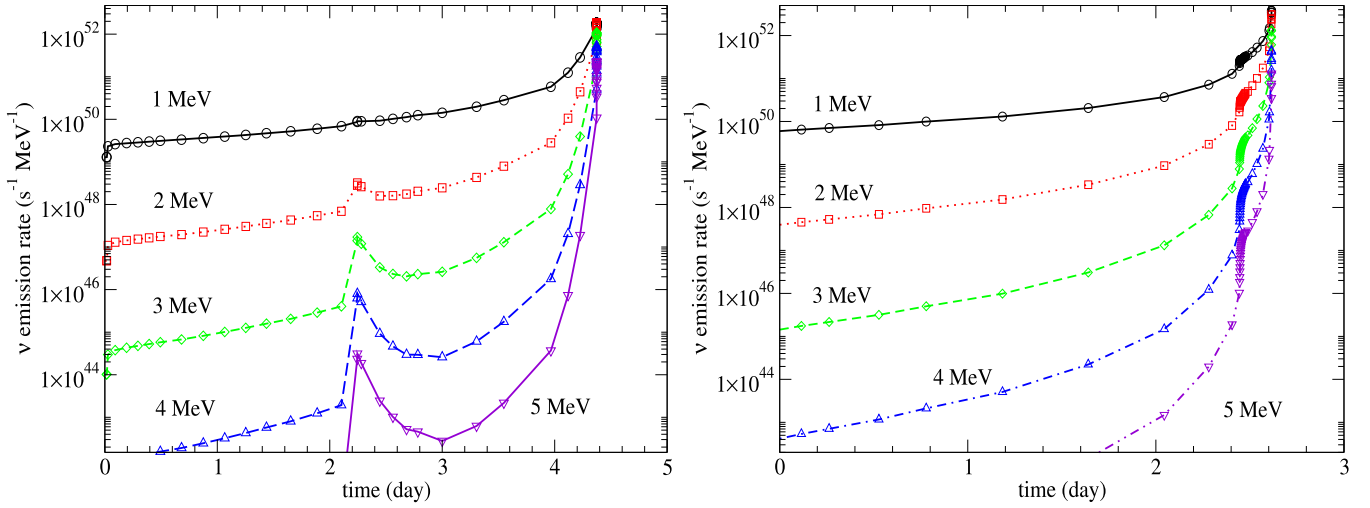


Figure 8. (Left panel) Neutrino spectral time evolution for ν_e from 1 to 5 MeV before collapse in model He40A. (right panel). Same as the left panel but for model He62A. The time convention follows Figure 7.

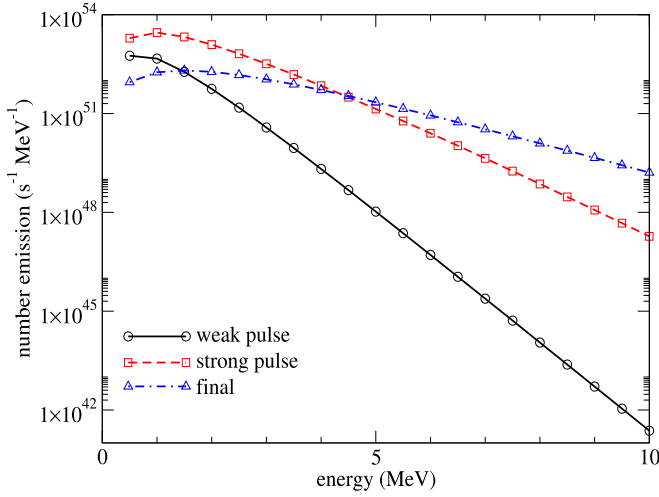


Figure 9. Neutrino spectral snapshots of model He40A for three moments: at the neutrino emission peaks during the second pulse (weak pulse), the sixth pulse (strong pulse), and near the end of the simulation.

Table 3

Nearby Massive Stars That Have a Distance below 10 kpc and a Mass above $80 M_{\odot}$

Star	Mass	Distance	References
Cygnus OB2-12	110	1.6	Oskinova et al. (2017), Camarillo et al. (2018)
HD 93129 A	110	2.3	Cohen et al. (2011)
η Carinae A	~ 100	2.3	Walborn (2012), Kashi & Soker (2010)
Cygnus OB2 #516	100	1.4	Herrero et al. (2002)

Note. Mass is in unit of M_{\odot} . Distance is in unit of kpc.

Thermal processes include such as pair-neutrino in the thermalized core, in particular in regions where complete burning proceeds (burning of matter until nuclear statistical equilibrium is reached). Electron captures occur mostly in the burnt matter in NSE with a high density ($\sim 10^9 \text{ g cm}^{-3}$). In this density range, electrons become extremely degenerate with a high Fermi energy, which may exceed the mass-energy difference between a neutron and a proton. This favors the capture of electrons on the nuclei and

results in ν_e emission. Computation of electron capture in these supernova is important for a self-consistent computation. See, for example, Seitzzahl et al. (2009) for the local electron capture rate for stars undergoing thermonuclear explosions and Jones et al. (2016), Leung & Nomoto (2018), Leung & Nomoto (2019), and Leung et al. (2019b) for recent SN Ia simulations including electron captures. Depending on the explosion mechanisms, the runaway can propagate in the form of sub-sonic deflagration or supersonic detonation. In both cases, the burnt ash can reach the temperature $\sim 5\text{--}9 \times 10^9 \text{ K}$, where matter achieves nuclear statistical equilibrium. In Odrzywolek & Plewa (2011), Leung et al. (2015), and Wright et al. (2017b), neutrino production is analyzed for pure turbulent deflagration (PTD), turbulent deflagration model with deflagration-detonation transition (DDT), and gravitationally confined detonation (GCD) models. The time evolution of neutrinos is sensitive to the explosion mechanism; for example, the one-peak structure for the PTD model versus the two-peak structure in the DDT and GCD models. In all models, they have the lowest neutrino luminosity and possible counts in major representative neutrino detectors. But they have an intermediate averaged neutrino energy.

A PISN also shares a similar neutrino production mechanism because of its thermonuclear origin. Different from an SN Ia, the much more massive hot core $2\text{--}4 M_{\odot}$ can generate more ^{56}Ni before it is completely disrupted. In Wright et al. (2017a), the neutrino emission signal is also analyzed.

CCSN has completely different neutrino production mechanisms by electron capture and neutron star cooling processes, such as the URCA process. Prior to its collapse, the deleptonization via $e^- + {}^A_Z X \rightarrow {}^A_{Z-1} X' + \nu_e$ and thermal neutrinos contribute to neutrino cooling. The thermally excited core is also about $10^9\text{--}10^{10} \text{ K}$ when the core reaches $10^{10} \text{ g cm}^{-3}$. In Yoshida et al. (2016a), the neutrino signals from 12 to $20 M_{\odot}$ stars are studied. The neutrino generation is, in general, monotonically increasing in time before its collapse. The massive star has a lower neutrino luminosity but still a significant detection count. This is because the precollapse phase also includes the hydrostatic Si-burning, which can take place ~ 1 day where the core reaches above $>10^9 \text{ K}$ before the onset of collapse.

We remark that even though the SN Ia explodes in a similar manner comparable to the pulsation mechanism in PPISN and

Table 4
Optimistic Total Neutrino Number Detection Count to Be Received by Terrestrial Neutrino Detectors

Model	Mass	He40A	He45A	He50A	He55A	He55A	He60A	He60A	He62A	He62A
Pulse		1–6	1–4	1–2	2	3	1	2	1	2
KamLAND	1.0	2	< 1	< 1	< 1	< 1	< 1	< 1	< 1	< 1
SNO+	0.78	1	< 1	< 1	< 1	< 1	< 1	< 1	< 1	< 1
Borexino	0.278	< 1	< 1	< 1	< 1	< 1	< 1	< 1	< 1	< 1
JUNO	20	36	8	4	2	2	< 1	1	< 1	1
RENO-50	18	32	7	3	2	1	< 1	1	< 1	1
LENA	50	90	20	9	6	4	1	3	1	3
Super-Kamiokande (with Gd)	32.5	40	9	4	3	2	< 1	1	< 1	1
Hyper-Kamiokande (with Gd)	220	680	150	72	43	29	7	20	6	20
DUNE	40	36	8	4	2	2	< 1	1	< 1	1

Note. Masses of the detector are in units of kT. The star model is assumed to be at 1 kpc from the Earth. We refer the readers to Paper I for a detailed description of each pulse.

also PISN, it has a much lower detection count for three reasons.

First, the mass inside the star that can efficiently generate neutrinos, in particular the pair-neutrino, is much lower than the latter two cases. The maximum mass it can incinerate is the Chandrasekhar mass ($\sim 1.4 M_{\odot}$) or about $1 M_{\odot}$ for the sub-Chandrasekhar mass case. On the other hand, in a PISN or a PPISN, the amount of mass capable of incinerating ^{16}O and that reaches above 10^9 K can range from a few to $\sim 30 M_{\odot}$.

Second, the timescale for the star to emit neutrino is much longer in a PPISN and a PISN, compared to an SN Ia. In an SN Ia, from the incineration to the expansion, the time duration where the matter reaches the temperature above 10^9 K is less than 1–2 s, which is the typical time for the deflagration and detonation wave to sweep across the star and disrupt the star. On the other hand, due to a longer dynamical timescale (≥ 100 – 1000 s), the total number of neutrinos emitted by PPISN and PISN can be much higher.

Third, the typical density in SNe Ia is much higher in the Chandrasekhar mass scenario. The central density is about 10^9 g cm^{-3} (although variation exists as indicated from different SN Ia observations (Nomoto & Leung 2017a; Leung & Nomoto 2018) and from the progenitor (Nomoto & Leung 2018)). The strong degeneracy limits the emission rate. Notice that the thermal neutrinos can also be emitted strongly during the nuclear runaway phase in the electron capture supernova (Nomoto & Hashimoto 1988; Doherty et al. 2015; Leung & Nomoto 2017, 2019; also applies for ONeMg core). Before the star collapses into a neutron star, the O–Ne deflagration also allows the matter to reach $\sim 10^9$ K (Leung et al. 2019b). Furthermore, the pre-runaway electron captures by ^{20}Ne and ^{24}Mg provide another channel for producing neutrinos other than thermal neutrinos (Nomoto & Leung 2017b; Suzuki et al. 2019; Zha et al. 2019).

4.3. Conclusion

In this article, we extended our previous study of PPISNe to examine the associated neutrino signals. In Leung & Nomoto (2018), we performed one-dimensional stellar evolutionary simulations of this class of supernovae using the one-dimensional stellar evolution code MESA version 8118. We followed the evolution of the He core from the main-sequence phase until the collapse of the star. Meanwhile, we recorded the

thermodynamic trajectories of the star to later be able to analyze its neutrino emission (done in this work).

We use the neutrino subroutine *sneut5*⁷ for calculating the detailed neutrino emission of the He core models of mass 40–64 M_{\odot} . We follow their neutrino emission history from the onset of pulsation until its collapse. We further extract its spectra by the semi-analytic formulae of pair- and plasmon-neutrinos. We analyzed the possible neutrino observables for He cores from 40 to 64 M_{\odot} . They correspond to the main-sequence stars of masses ~ 80 – $140 M_{\odot}$ (but with metallicity dependence). We find that neutrinos are mostly produced by the pair-neutrino channel ($e^- + e^+ \rightarrow \nu_e + \bar{\nu}_e$). Most of these neutrinos are emitted within the one hour during its contraction prior to its pulsational mass loss. The lower-mass star tends to emit more neutrinos and has higher detection counts because it is more compact. Due to its thermal nature, the neutrinos have an averaged energy of about a few MeV. At last, using the pair-neutrino as an example, we confirm that the current analytic approximation formula of neutrino production (Itoh et al. 1994) can well match the more updated neutrino luminosity table given in Odrzywolek (2007).

This work shows that the repeated pulsations of PPISN allow the star to reach the hot and compact state more frequently than its more massive relative (pair-instability supernova) and less massive relative (CCSN). This provides additional opportunities to predict its collapse by detecting its neutrinos. Future detection of these neutrinos may serve as an early warning signal for the optical telescopes to detect the electromagnetic wave signals coming from the early shock breakout. Those neutrinos contain precious information about the pre-explosion stellar structure.

This work has been supported by the World Premier International Research Center Initiative (WPI Initiative), MEXT, Japan, and JSPS KAKENHI grant Nos. JP17K05382 and 26104007 (Kakenhi). Work by S.B. on PPISN is supported by the Russian Science Foundation grant 19-12-00229. S.C.L. also acknowledges support by funding from HST-AR-15021.001-A. We thank F. X. Timmes for his open-source microphysics algorithm including the Helmholtz equation of state subroutine and the neutrino subroutine *sneut5*. We also

⁷ Open-source subroutine available on http://cococubed.asu.edu/code_pages/nuloss.shtml. The subroutine summarizes the parameterized neutrino emission rates in works including Itoh et al. (1996).

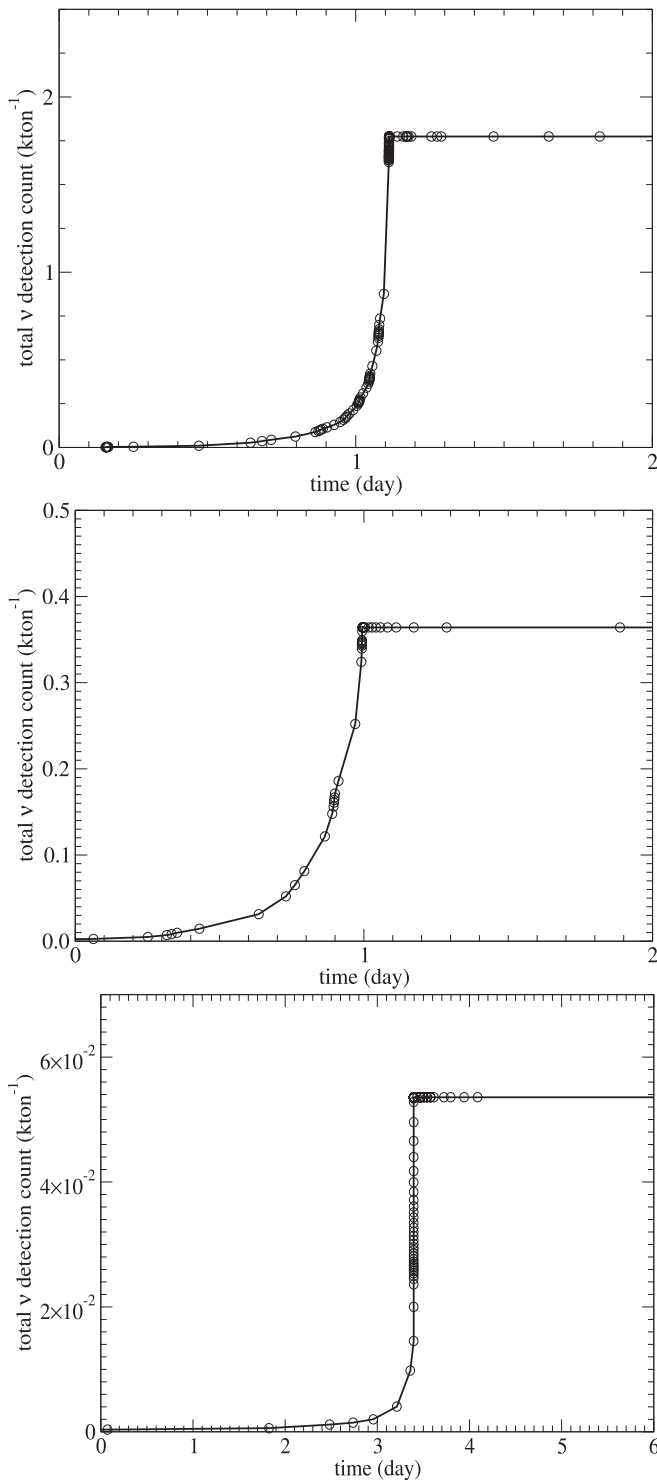


Figure 10. (Top panel) Cumulative ν_e count against time for ν_e and ν_τ of model He40A. Notice that the unit here are kton^{-1} . The neutrino detector is assumed to have a mass of 1 kton and is located at 1 kpc from the supernova. (Middle panel) Same as top panel but for model He50A. (Bottom panel) Same as top panel but at the peak of the second pulse for model He62A. Time zero is shifted so that the relevant time period can be shown directly.

thank A. Odrzywolek for supplying the open-source pair-neutrino table for cross-checking with other approximation formula. We also thank Professor Mark Vagins for the informative introduction on the neutrino detection techniques and guidance in the Super-Kamiokande and KamLAND detection site.

Table 5
Typical Neutrino Properties from Different Types of Supernovae

Supernova	L_{peak}	E_ν	$N_{\nu(S)}$	$N_{\nu(H)}$
Type Ia (PTD) ^a	10^{49}	3.8	0.063	0.106
Type Ia (DDT) ^b	10^{49}	3.5	0.013	0.220
Type Ia (GCD) ^c	10^{47}	0.5/3	0.0024	0.0267
ONeMg core ^d	10^{46}	1–2	<1	<1
Massive star ($M = 15M_\odot$) ^e	10^{47}	2.0	15	250
PPISN ($M_{\text{He}} = 40M_\odot$)	10^{47}	1.5	0.403	6.80
PPISN ($M_{\text{He}} = 62M_\odot$)	10^{47}	1.0	0.0102	0.203
PISN ($M = 250M_\odot$) ^f	10^{50}	2	6.98	52.23

Notes. Neutrino luminosity at peak L_{peak} is in units of erg s^{-1} and neutrino energy E_ν is in units of MeV. Neutrino Count $N_{\nu(i)}$ is the number of neutrinos expected to be detected by Super-Kamiokande (i) = (S) and Hyper-Kamiokande (i) = (H) when the explosion occurs 10 kpc away from the Earth. For SN II, we only choose the neutrino luminosity and energy before its collapse for a better comparison with PPISN and PISN where the thermal neutrino is the main component. “Massive star” includes the neutrino emission before the onset of its Fe-core collapse.

^a Odrzywolek et al. (2004).

^b Odrzywolek et al. (2004).

^c Wright et al. (2017b).

^d Kato et al. (2015).

^e Yoshida et al. (2016b).

^f Wright et al. (2017a).

Appendix

Use of Analytic Approximation for Neutrino Luminosity

In the main text, we studied the neutrino emission based on the implicit subroutine included in MESA for the neutrino light curve⁸ and some analytic approximations for the neutrino spectra (Odrzywolek 2007). The subroutine summarized the analytic approximations presented in Itoh et al. (1994), with the detailed calculation described in Itoh et al. (1989). The subroutine *sneut4* and *sneut5* correspond to the same input physics but for the single and double precisions. The subroutine has been widely applied to many applications in stellar astrophysics. However, with the more detailed calculations in some of the neutrino processes (e.g., Misiasek et al. 2006; Odrzywolek 2007), it is unclear whether this approximation remains fully accurate. To check its accuracy, we compare the neutrino luminosity from pair-production. This process is the most important neutrino production channel for massive stars due to its low density–high temperature core. To compare with, we use the neutrino table⁹ and the analytic formula given in Blinnikov & Rudzkii (1989).

In Figure 11, we compare the pair-neutrino luminosity at different densities from 1 to $10^{10} \text{ g cm}^{-3}$ and different temperatures 10^8 – 10^{10} K. At a low density, the two curves overlap with each other, showing that at the low density–high temperature regime, the analytic formula is a very good approximation compared to the exact values presented in table form. This is important because this is a typical temperature and density similar to that during the pair-creation instabilities in most stellar models. This guarantees the accuracy of neutrino energy loss in the presupernova evolution.

In an intermediate density ($\sim 10^{5.5} \text{ g cm}^{-3}$, the two curves still overlap well except at low temperature around 10^8 K, where the discrepancy is within one order of magnitude. Above

⁸ http://cococubed.asu.edu/code_pages/nuloss.shtml

⁹ <http://th.if.uj.edu.pl/~odrzywolek/psns/index.html>

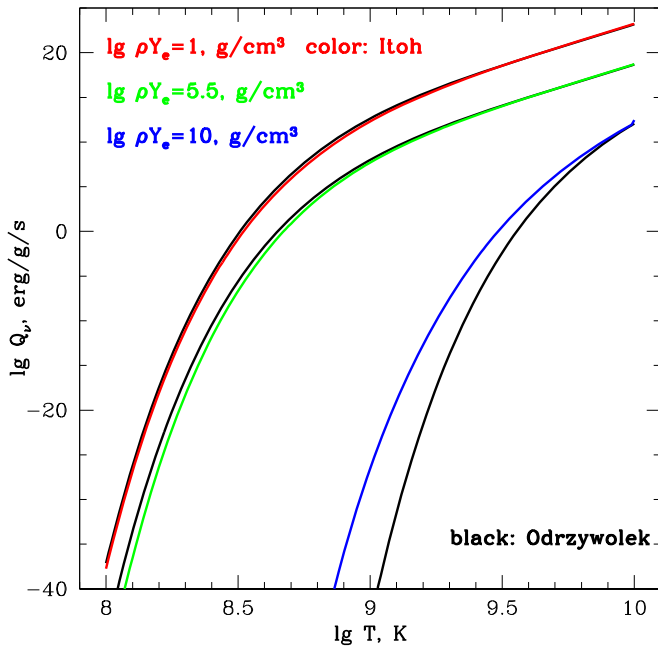


Figure 11. Comparison between the analytic formula for the pair-neutrino production used in the MESA code and the table based on Odrzywolek (2007). The black line corresponds to the numerical data from the table and the colored lines correspond to those from the analytic formulas.

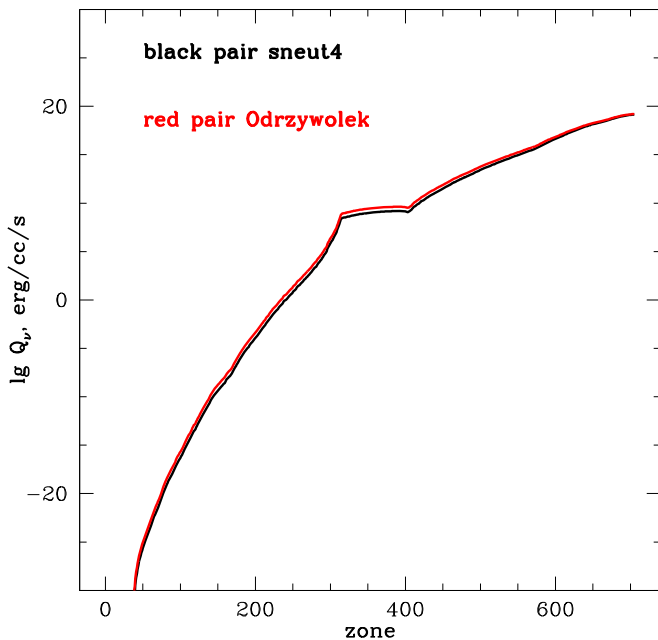


Figure 12. Comparison between the analytic formula (black line) for the pair-neutrino used in the MESA code and the table (red line) based on Odrzywolek (2007) for the PPISN model He60A. The stellar profile is obtained at the most compact state in the first pulse.

10^9 K, the formula agrees very well with the table. We remark that at that density range, the pair neutrino is less important.

At high density ($\sim 10^{10}$ g cm $^{-3}$), the discrepancy becomes much larger at low temperatures. The discrepancy is less severe at a temperature $10^{9.5}$ K, but below that, the error grows when temperature drops. The discrepancy can be as large as ten orders of magnitude. Again, the large discrepancy does not affect the total neutrino calculation because at such high

density, the photoneutrino and electron bremsstrahlung are the major channels for the neutrino production.

From the three regimes, it suffices to conclude that for the current neutrino calculation, the analytic approximation of the pair-neutrino mechanism can very well describe the neutron luminosity.

At last, we apply this comparison to a specific stellar profile obtained from our calculations. We use model He60A as an example. We input the temperature, density, and composition obtained from the profile and then compare the corresponding pair-neutrino luminosity at different positions in the star. The profile is taken from the model when the star obtained its highest central density during the first pulse. In Figure 12, we plot the neutrino luminosity profiles computed by the subroutine and by the table. In the core (within zone 400), due to the high central density, the electron matter becomes degenerate, which suppresses the pair-neutrino. Despite that, the high temperature in the core provides the condition where the analytic formula agrees very well with the table values. Outside the core, when the pair-neutrino becomes important, the two methods still agree well with each other. This shows that in the typical stellar calculation, the analytic approximations can still very well reproduce the neutrino luminosity calculated from more accurate ones by direct table interpolation.

ORCID iDs

Shing-Chi Leung <https://orcid.org/0000-0002-4972-3803>
 Sergei Blinnikov <https://orcid.org/0000-0002-5726-538X>
 Koji Ishidoshiro <https://orcid.org/0000-0001-9271-2301>
 Alexandre Kozlov <https://orcid.org/0000-0002-6679-3985>
 Ken'ichi Nomoto <https://orcid.org/0000-0001-9553-0685>

References

- Aalbers, J., Agostini, F., Alfonsi, M., et al. 2016, *JCAP*, 2016, 017
 Aalseth, C. E., Acerbi, F., Agnes, P., et al. 2018, *EPJP*, 133, 131
 Aartsen, M. G., Abraham, K., Ackermann, M., et al. 2016, *ApJL*, 824, L28
 Abbasi, R., Abdou, Y., Abu-Zayyad, T., et al. 2011, *A&A*, 535, A109
 Abe, H.-K. C. K., Abe, T., Aihara, Y., et al. 2011a, arXiv:1109.3262
 Abe, K., Hayato, Y., Iida, T., et al. 2011b, *PhRvD*, 83, 052010
 Acciarri, D. C. R., Acero, M. A., Adamowski, M., et al. 2016, arXiv:1601.05471
 Agostini, M., Appel, S., Bellini, G., et al. 2015, *PhRvD*, 92, 031101(R)
 An, F., An, G., An, Q., et al. 2016, *JPhG*, 43, 030401
 Andringa, S. C. S., SNO+ Collaboration, et al. 2016, *JPhCS*, 665, 012080
 Antonoli, P., Tresch Fienberg, R., Fleurot, R., et al. 2004, *NJPh*, 6, 114
 Asakura, K., Gando, A., Gando, Y., et al. 2016, *ApJ*, 818, 91
 Barkat, Z., Rakavy, G., & Sack, N. 1967, *PhRvL*, 18, 379
 Beacom, J. F., & Vagins, M. R. 2004, *PhRvL*, 93, 171101
 Belczynski, K., Ryu, T., Perna, R., et al. 2017, *MNRAS*, 471, 4702
 Bellini, G., Benziger, J., Bick, D., et al. 2014, *PhRvD*, 89, 112007
 Bersten, M. C., Folatelli, G., García, F., et al. 2018, *Natur*, 554, 497
 Blinnikov, S. I., & Rudzskii, M. A. 1989, *SvA*, 33, 377
 Brdar, V., Lindner, M., & Xu, X.-J. 2018, *JCAP*, 2018, 025
 Bykov, A. M., Ellison, D. C., Gladilin, P. E., & Osipov, S. M. 2015, *MNRAS*, 453, 113
 Camarillo, T., Mathur, V., Mitchell, T., & Ratra, B. 2018, *PASP*, 130, 024101
 Chen, K.-J., Woosley, S., Heger, A., Almgren, A., & Whalen, D. J. 2014, *ApJ*, 792, 28
 Cohen, D. H., Gagné, M., Leutenegger, M. A., et al. 2011, *MNRAS*, 415, 3354
 Dessart, L., John Hillier, D., & Audit, E. 2017, *A&A*, 605, A83
 Doherty, C. L., Gil-Pons, P., Siess, L., Lattanzio, J. C., & Lau, H. H. B. 2015, *MNRAS*, 446, 2599
 Gamavich, P. M., Tucker, B. E., Rest, A., et al. 2016, *ApJ*, 820, 23
 Heger, A., & Woosley, S. E. 2002, *ApJ*, 567, 532
 Herrero, A., Puls, J., & Najarro, F. 2002, *A&A*, 396, 949

- Hirschi, R. 2017, in *Handbook of Supernovae*, ed. A. W. Alsabti & P. Murdin (Cham: Springer), 567
- Itoh, N., Adachi, N., Nakagawa, M., Kohyama, Y., & Munakata, H. 1989, *ApJ*, 339, 354
- Itoh, N., Hayashi, H., Nishikawa, A., & Kohyama, Y. 1994, *ApJS*, 102, 411
- Itoh, N., Hayashi, H., Nishikawa, A., & Kohyama, Y. 1996, *ApJS*, 102, 411
- Jones, S., Röpke, F. K., Pakmor, R., et al. 2016, *A&A*, 593, A72
- Kashi, A., & Soker, N. 2010, *ApJ*, 723, 602
- Kato, C., Delfan Azari, M., Yamada, S., et al. 2015, *ApJ*, 808, 168
- Kunugise, T., & Iwamoto, K. 2007, *PASJ*, 59, L57
- Leung, S.-C., Chu, M.-C., & Lin, L.-M. 2015, *MNRAS*, 454, 1238
- Leung, S.-C., & Nomoto, K. 2017, *MmSAI*, 88, 266
- Leung, S.-C., & Nomoto, K. 2018, *ApJ*, 861, 143
- Leung, S.-C., & Nomoto, K. 2019, *PASA*, 36, e006
- Leung, S.-C., Nomoto, K., & Blinnikov, S. 2019a, *ApJ*, 887, 72
- Leung, S.-C., Nomoto, K., & Suzuki, T. 2019b, arXiv:1901.11438
- Limongi, M. 2017, in *Handbook of Supernovae*, ed. A. W. Alsabti & P. Murdin (Cham: Springer), 513
- Marchant, P., Renzo, M., Farmer, R., et al. 2019, *ApJ*, 882, 36
- Misiaszek, M., Odrzywolek, A., & Kutschera, M. 2006, *PhRvD*, 74, 043006
- Nomoto, K., & Hashimoto, M. 1988, *PhR*, 163, 13
- Nomoto, K., & Leung, S.-C. 2017a, in *Handbook of Supernovae*, ed. A. W. Alsabti & P. Murdin (Cham: Springer), 1275
- Nomoto, K., & Leung, S.-C. 2017b, in *Handbook of Supernovae*, ed. A. W. Alsabti & P. Murdin (Cham: Springer), 483
- Nomoto, K., & Leung, S.-C. 2018, *SSRv*, 214, 67
- Odrzywolek, A. 2007, *EPJC*, 52, 425
- Odrzywolek, A., Misiaszek, M., & Kutschera, M. 2004, *Aph*, 21, 303
- Odrzywolek, A., & Plewa, T. 2011, *A&A*, 529, A156
- Ohkubo, T., Nomoto, K., Umeda, H., Yoshida, N., & Tsuruta, S. 2009, *ApJ*, 706, 1184
- Oskinova, L. M., Huenemoerder, D. P., Hamann, W. R., et al. 2017, *ApJ*, 845, 39
- Owocki, S. P., Hirai, R., Podsiadlowski, P., & Schneider, F. R. N. 2019, *MNRAS*, 485, 988
- Paxton, B., Bildsten, L., Dotter, A., et al. 2011, *ApJS*, 192, 3
- Paxton, B., Cantiello, M., Arras, P., et al. 2013, *ApJS*, 208, 4
- Paxton, B., Marchant, P., Schwab, J., et al. 2015, *ApJS*, 220, 15
- Paxton, B., Schwab, J., Bauer, E. V., et al. 2017, *ApJS*, 234, 34
- Raj, N. 2019, arXiv:1907.05533
- Raj, N., Takhistov, V., & Witte, S. J. 2019, arXiv:1905.09283
- Seitenzahl, I. R., Townsley, D. M., Peng, F., & Truran, J. W. 2009, *ADNDT*, 95, 96
- Seo, H. 2015, in *Proc. XVI Int. Workshop on Neutrino Telescopes (NEUTEL15)* (SISSA) (Istituto Veneto, Italy), 83
- Simpson, C., Abe, K., Bronner, C., et al. 2019, *ApJ*, 885, 133
- Sorokina, E., Blinnikov, S., Nomoto, K., Quimby, R., & Tolstov, A. 2016, *ApJ*, 829, 17
- Suwa, Y., Sumiyoshi, K., Nakazato, K., et al. 2019, *ApJ*, 881, 139
- Suzuki, A. 1999, *NuPhS*, 77, 171
- Suzuki, T., Zha, S., Leung, S.-C., & Nomoto, K. 2019, *ApJ*, 881, 64
- Tolstov, A., Nomoto, K., Blinnikov, S., et al. 2017, *ApJ*, 835, 266
- Walborn, N. R. 2012, in *The Company Eta Carinae Keeps: Stellar and Interstellar Content of the Carina Nebula*, ed. K. Davidson & R. M. Humphreys (Boston, MA: Springer US), 25
- Watanabe, H., Zhang, H., Abe, K., et al. 2009, *Aph*, 31, 320
- Woosley, S. E. 2017, *ApJ*, 836, 244
- Woosley, S. E. 2018, *ApJ*, 863, 105
- Wright, W. P., Glimmer, M. S., Froehlich, C., & Kneller, J. P. 2017a, *PhRvD*, 96, 103008
- Wright, W. P., Kneller, J. P., Ohlmann, S. T., et al. 2017b, *PhRvD*, 95, 043006
- Wright, W. P., Nagaraj, G., Kneller, J. P., Scholberg, K., & Seitenzahl, I. R. 2016, *PhRvD*, 94, 025026
- Wurm, M., Bick, D., Enqvist, T., et al. 2015, *PhPro*, 61, 376
- Wurm, M., Beacom, J. F., Bezrukov, L. B., et al. 2012, *Aph*, 35, 685
- Yoshida, T., Takahashi, K., Umeda, H., & Ishidoshiro, K. 2016a, *PhRvD*, 93, 123012
- Yoshida, T., Umeda, H., Maeda, K., & Ishii, T. 2016b, *MNRAS*, 457, 351
- Zha, S., Leung, S.-C., Suzuki, T., & Nomoto, K. 2019, *ApJ*, 886, 22